Zhang et al. *Zool. Res.* 2026, 47(5): 1613−1625
https://doi.org/10.24272/j.issn.2095-8137.2026.321
https://cstr.cn/32248.14.zr.2026.321

ZR | Zoological Research

Article Open Access

Functional heterogeneity of mouse fetal liver hematopoietic stem cells revealed by clonal lineage tracing and single-cell transcriptomics

Man Zhang[1,#], Yanli Ni[1,#], Di Liu[2,#], Dong Xiang[3,4,#], Gaoke Liu[5], Jie Zhou[1], Yu Lan[3,4], Bing Liu[1,*], Zongcheng Li[1,*]

[1] *State Key Laboratory of Experimental Hematology*, *Haihe Laboratory of Cell Ecosystem*, *Senior Department of Hematology*, *Chinese PLA General Hospital*, *Beijing* 100071, *China*

[2] *Department of Neurology*, *Xuanwu Hospital Capital Medical University*, *National Center for Neurological Disorders*, *Beijing* 100053, *China*

[3] *State Key Laboratory of Experimental Hematology*, *National Clinical Research Center for Blood Diseases*, *Haihe Laboratory of Cell Ecosystem*, *Institute of Hematology & Blood Diseases Hospital*, *Chinese Academy of Medical Sciences & Peking Union Medical College*, *Tianjin* 300020, *China*

[4] *Tianjin Institutes of Health Science*, *Tianjin* 301600, *China*

[5] *Department of Medical Genetics*, *College of Basic Medical Science*, *Army Medical University (Third Military Medical University)*, *Chongqing* 400038, *China*

ABSTRACT

The relationship between lineage output and transcriptional features of hematopoietic stem cells (HSCs) has been reported in adult bone marrow, yet it remains unclear in fetal liver, given their distinct developmental stage and microenvironment. Here, we systematically characterized the functions of E14.5 mouse fetal liver HSCs by lentiviral barcode labeling followed by transplantation, with subsequent single-cell RNA sequencing (scRNA-seq) and clonal analysis performed on donor-derived HSCs and their progeny in recipient bone marrow. We identified three HSC subtypes based on lineage bias, with myeloid-biased and balanced subtypes predominating. Importantly, within the same subtype, HSCs and their progeny share several transcriptional programs, and these programs show minimal overlap between subtypes. We term the retention of subtype-specific transcriptional features across lineages as “transcriptional persistence”. Notably, this phenomenon was not observed in adult bone marrow. Alternatively, classification by progeny output activity revealed the presence of low-output and high-output subtypes within fetal liver HSCs. Although these two subtypes showed no significant difference in stemness features, they exhibited distinct transcriptional features and signaling activation states, which also differed from their counterparts in bone marrow, indicating that the biological characteristics of HSCs with different output activities vary by developmental stage. Of note, in both fetal liver and adult bone marrow, transcriptional persistence showed no obvious correlation with output activity, suggesting a specific coupling relationship between transcriptional persistence and lineage bias. Collectively, our study provides a clonal-resolution view of fetal liver HSC heterogeneity, enhancing our understanding of HSC diversity across different developmental stages.

Keywords: Fetal liver; Hematopoietic stem cell; Clonal lineagetracing; Transcriptional persistence; Heterogeneity

INTRODUCTION

Hematopoietic stem cells (HSCs) are rare, self-renewing cells at the apex of the hematopoietic hierarchy capable of multilineage differentiation (Crisan & Dzierzak, 2016). Many studies using refined cell sorting, limiting dilution, single-cell transplantation, and genetic lineage tracing (Cheng et al., 2020; Crisan & Dzierzak, 2016; Laurenti & Göttgens, 2018) have shown that the HSC compartment is heterogeneous in surface marker phenotype (Wilson et al., 2015), cell cycle status (Wilson et al., 2008), reconstitution kinetics (Benz et al., 2012; Dykstra et al., 2007; Muller-Sieburg et al., 2012), self-renewal capacity (Ema et al., 2014), and lineage output bias after transplantation (Benz et al., 2012; Dykstra et al., 2007;

Received: 13 July 2026; Accepted: 04 August 2026; Online: 05 August 2026

Foundation items: This work was supported by the National Key R&D Program of China (2021YFA1100901, 2022YFA1105700, 2022YFA1103501, 2021YFA1100102), National Natural Science Foundation of China (82270118, 82330006, 82470115), and China Postdoctoral Science Foundation (2024M764308)

[#]Authors contributed equally to this work

*Corresponding authors, E-mail: bingliu17@126.com; lizc07@126.com

Muller-Sieburg et al., 2012; Pei et al., 2020; Rodriguez-Fraticelli et al., 2020). This heterogeneity complicates our understanding of HSC function in health and disease (Yi et al., 2026), making it critical to comprehensively delineate HSC heterogeneity to better elucidate HSC biology across developmental stages and to improve hematopoietic stem cell transplantation.

It is widely accepted that the fetal liver is the major site of HSC expansion (Ema & Nakauchi, 2000) and maturation (Ganuza et al., 2022; Kieusseian et al., 2012) before birth and that fetal liver HSCs differ substantially from adult bone marrow HSCs (Crisan et al., 2015; Kristiansen et al., 2016; Morrison et al., 1995; Rebel et al., 1996; Zhang et al., 2024). Identifying the functional and molecular characteristics of distinct fetal liver HSC subtypes may provide a theoretical foundation for clinically guided selective expansion of specific stem cell subsets. Through single-cell transplantation of E14.5 fetal liver HSCs ($CD45^+CD201^+CD48^-CD150^+$), the Eaves group classified HSCs into α-HSC (lymphoid-deficient), β-HSC (balanced), and γ/δ-HSC (myeloid-deficient) based on lineage output, and demonstrated that only α- and β-HSC clones possess long-term reconstitution and self-renewal ability, together accounting for approximately 50% of the population, in contrast to approximately 80% in adult bone marrow (Benz et al., 2012; Dykstra et al., 2007). Moreover, the heterogeneity of lineage-biased output can be traced back to the hematopoietic stem cell precursor stage (Ye et al., 2017). However, the molecular features of these functional subtypes remain largely unknown. More recently, Stonehouse and colleagues employed lentiviral DNA barcoding to label E14.5 fetal liver HSCs and assessed their clonal contribution to mature lineages two weeks after transplantation (Stonehouse et al., 2024). They found that over 30% of clones produced multilineage output, while the rest gave rise to various combinations of restricted multilineage outputs, erythro-myeloid restriction, or single-lineage restriction (Stonehouse et al., 2024). Despite its throughput advantages, this barcoding method does not capture transcriptional information, leaving unanswered the critical question: do HSC clones with distinct lineage differentiation capacities exhibit differences at the transcriptional level? If so, where do these clones with different lineage output functions reside within the transcriptional landscape?

Single-cell transcriptomics has offered new perspectives on the molecular features of fetal liver HSCs, but predominantly along developmental timelines rather than across functional subtypes. For instance, it has been shown that E16.5 fetal liver and P7 bone marrow HSCs cluster separately, whereas P0 bone marrow and fetal liver-derived HSCs are predicted to belong to the same cluster, with P0-derived HSCs co-expressing embryonic and adult transcripts and possessing an adult-like transcriptomic signature score (Li et al., 2020). This fetal-to-adult transcriptomic transition occurs gradually along a continuous timeline, with adult-specific regulators being progressively activated during development (Bunis et al., 2021). However, these studies remain limited to transcriptomic descriptions alone and do not link molecular states to functional output, particularly at the clonal level.

To overcome these limitations, we employed the Lineage and RNA recovery (LARRY) platform, which integrates lentiviral barcode tracing with single-cell transcriptomics, enabling simultaneous capture of lineage fate and molecular state at single-cell resolution (Rodriguez-Fraticelli et al., 2020; Weinreb et al., 2020). Using this technique, the Camargo group identified that adult bone marrow HSCs can be divided into low-output and high-output clones based on progeny output activity, and into megakaryocyte-biased (Mk-biased) and multilineage HSCs based on lineage bias (Rodriguez-Fraticelli et al., 2020). Additionally, secondary transplantation experiments showed that low-output clones maintain long-term stable reconstitution capacity. Whether fetal liver HSCs contain similar functional subtypes and what molecular features distinguish them remains to be answered.

In this study, we applied the LARRY system to investigate the functional heterogeneity of mouse fetal liver HSCs. We systematically revealed multiple clonal subtypes and their distinct transcriptomic features. We further demonstrated both shared and distinct characteristics between fetal liver and adult bone marrow HSCs in clonal composition and molecular signatures. This study enriches our understanding of the functional heterogeneity of fetal liver HSCs and provides insights that may inform future efforts to improve in vitro HSC regeneration.

MATERIALS AND METHODS

Mouse

Mice were housed in the Laboratory Animal Center of the Academy of Military Medical Sciences in accordance with institutional guidelines. Mouse experiments were approved by the Institutional Animal Care and Use Committee of the Laboratory Animal Center (Approval No.: IACUC-DWZX-2021-056). All mice were maintained on the C57BL/6 background. Male (CD45.1/1) and female (CD45.2/2) mice were paired to generate CD45.1/2 embryos.

Tissue dissociation

Pregnant mice were euthanized, and fetal liver tissues were aseptically harvested and placed into α-MEM (Gibco, USA) with 10% fetal bovine serum (Hyclone, USA) medium, respectively. The fetal liver tissues were gently pipetted using a 1 mL disposable sterile syringe until no tissue clumps remained. The cells were washed twice with 2% FBS/PBS, followed by filtration and resuspension to obtain a single-cell suspension.

Bone marrow cells were obtained from the femurs, tibias, ilia, humeri, and ulnae of adult mice and treated with or without erythrocyte depletion using red blood cell lysis buffer (eBioscience, USA), respectively. Adult thymus and spleen tissues were processed by grinding to obtain single-cell suspensions.

Flow cytometry and antibodies

Cells were sorted and analyzed using fluorescence-activated cell sorting (FACS) on FACS Aria II and FACS Calibur flow cytometers (BD, USA). All data were analyzed using FlowJo v.10.8.1. Cells were stained with the following antibodies: PE-conjugated Kit (BD, 2B8, USA), APC-conjugated Sca1 (eBioscience, D7, USA), APC-conjugated CD201 (eBioscience, eBio1560, USA), Brilliant Violet 510-conjugated CD150 (Biolegend, TC15-12F12.2, USA), PE-conjugated CD150 (Biolegend, TC15-12F12.2, USA), APC-eflour780-conjugated CD48 (eBioscience, HM48-1, USA), FITC-conjugated CD48 (eBioscience, HM48-1, USA), PE/Cyanine7-conjugated CD127 (eBioscience, A7R34, USA), PE/Cyanine7-conjugated CD45 (eBioscience, 30-F11, USA), PE/Cyanine7-conjugated CD41 (eBioscience, eBioMWReg30, USA), APC-

conjugated CD45.1 (eBioscience, A20, USA), PE-conjugated CD45.2 (eBioscience, 104, USA), APC-eflour780-conjugated CD45.2 (eBioscience, 104, USA), PE/Cyanine7-conjugated Ly-6G/Ly-6C (Gr-1) (Biolegend, 1A8, USA), PE/Cyanine7-conjugated Mac-1 (eBioscience, M1/70, USA), APC/Cyanine7-conjugated CD3e (eBioscience, 145-2C11, USA), PE/Cyanine7-conjugated CD3 (eBioscience, 145-2C11, USA), eFluor450-conjugated B220 (eBioscience, RA3-6B2, USA), PE/Cyanine7-conjugated B220 (eBioscience, RA3-6B2, USA), Brilliant Violet 605-conjugated Ter119 (Biolegend, TER119, USA), PE/Cyanine7-conjugated Ter119 (eBioscience, TER119, USA), Brilliant Violet 605-conjugated CD4 (Biolegend, GK1.5, USA), PE/Cyanine7-conjugated CD8a (eBioscience, 53-6.7, USA), Biotin-conjugated Ter119 (eBioscience, TER119, USA), Biotin-conjugated Ly-6G/Ly-6C (eBioscience, RB6-8C5, USA), Biotin-conjugated CD19 (eBioscience, MB19-1, USA), Biotin-conjugated CD3e (eBioscience, 145-2C11, USA), and Streptavidin eFlour450 (eBioscience, USA). 7-Aminoactinomycin D (eBioscience, USA) was used to exclude dead cells.

Cell populations were defined by the following cell surface phenotypes: HSCs, $Lin^-Sca1^+Kit^+CD150^+CD48^-$; multipotent progenitors (MPPs), $Lin^-Sca1^+Kit^+CD150^-$; megakaryocyte progenitors (MkPs), $Lin^-Sca1^-Kit^+CD150^+CD41^+$; myeloid progenitors (MyPs), $Lin^-Sca1^-Kit^+CD150^-$; and common lymphoid progenitors (CLPs), $Lin^-Sca1^{low}Kit^{low}CD127^+$ in bone marrow. GM ($Gr\text{-}1^+Mac\text{-}1^+$), B cells ($B220^+$), and T cells ($CD3^+$) were identified in bone marrow, peripheral blood, and spleen. T cells ($CD4^+$, $CD8^+$, $CD4^+CD8^+$) were identified in the thymus. Erythroid cells ($Ter119^+$) and platelets ($CD41^+$) were identified in peripheral blood and bone marrow. The lineage cocktail consisted of CD3, CD19, Gr-1, and Ter119.

Cell culture and LARRY library

For cell culture, fetal liver HSCs were pre-stimulated for 2–4 h in Stemline II medium (Sigma, Germany) supplemented with 2 mmol/L glutamine (Hyclone, USA), 100 U/mL penicillin and 100 mg/mL streptomycin (Hyclone, USA), and hematopoietic cytokines (100 ng/mL SCF, 100 ng/mL IL-3, and 100 ng/mL Flt3L; PeproTech, USA). Wells were pre-coated with 40 μg/mL RetroNectin (Takara, Japan) and seeded with pre-stimulated HSCs in 100 μL medium. Lentivirus was added once with polybrene (8 μg/mL; Sigma, Germany). After 8 h of infection, HSCs were washed twice with 2% FBS/PBS and resuspended for transplantation.

The LARRY library used in this study was initially purchased as a plasmid from Addgene (Pooled Library #140024), and lentiviral production and packaging were subsequently performed by GENEWIZ.

Transplantation assay

Fetal liver HSCs (CD45.1/2) were collected and injected into 8–12-week-old female recipients (CD45.2/2) via the tail vein, along with 2×10^4 nucleated fresh bone marrow carrier cells (CD45.2/2) per recipient. Recipients were pre-treated with a split dose of 8 Gy γ-irradiation (^{60}Co). Peripheral blood cells of recipients were analyzed monthly by FACS to detect chimerism.

For secondary transplantation, bone marrow cells were harvested from the femurs, tibias, ilia, humeri, and ulnae by flushing the bones with 5% BSA/PBS using a 10 mL disposable sterile syringe. Following harvesting, bone marrow cells were filtered through a 40 μm cell strainer to remove bone fragments, and then erythrocytes were depleted using 1× red blood cell lysis buffer (eBioscience, USA). Half of the sorted HSCs were allocated for single-cell RNA sequencing (scRNA-seq), while the remaining HSCs were injected into 8–12-week-old female recipients (CD45.2/2) via the tail vein, along with 2×10^4 nucleated fresh bone marrow carrier cells (CD45.2/2) per recipient. Peripheral blood cells of recipients were analyzed monthly by FACS to detect chimerism.

Single-cell RNA sequencing library preparation, sequencing, and quality control

Green fluorescent protein $(GFP)^+$ cells carrying the LARRY barcode were sorted from primary recipient bone marrow. A defined mixture of long-term HSCs and other progenitor populations (MPPs, MyPs, MkPs, CLPs) was prepared to reconstruct the full hematopoietic stem and progenitor compartment. The exact cell numbers and mixing ratios are provided in Supplementary Table S1. The mixed cell suspension was processed using the 10× Genomics 3' scRNA-seq kit according to the manufacturer's protocol. Libraries were sequenced on an Illumina NovaSeq platform (paired-end 150 bp, USA).

Raw sequencing data were aligned to the mouse reference genome (mm10) using Cell Ranger (v.5.0.1) with default parameters for read alignment, gene annotation, and UMI counting. Downstream analyses were performed using Seurat (v.4.1.1). Cells with unique molecular identifier (UMI) counts between 2 000 and 80 000, number of detected genes >700, and mitochondrial UMI count proportion <10% were retained for further analysis. Doublets were subsequently identified and removed using DoubletFinder (v.2.0.3).

Data normalization was performed using the NormalizeData function. The top 2 000 highly variable genes were identified with FindVariableFeatures. To minimize the influence of cell cycle heterogeneity on downstream analyses, we performed cell cycle scoring using Seurat's CellCycleScoring function (with the updated 2019 cell cycle gene list). For each gene in the initial set of variable genes, we calculated its absolute Pearson correlation coefficient with both the S.Score and the G2M.Score. A gene was retained as a high-variability feature only if the maximum of these two absolute correlation values was less than 0.3. Genes exceeding this threshold (i.e., those strongly correlated with either cell cycle phase) were removed from the variable gene set. This filtering step can effectively exclude cell-cycle-associated genes from subsequent dimensionality reduction and clustering. The filtered variable gene set was then used for scaling and principal component analysis. To correct for batch effects among different recipients, we applied the IntegrateLayers function with the RPCAIntegration method. The first 20 integrated principal components were selected for UMAP dimensionality reduction and Louvain clustering. Finally, we integrated unsupervised clustering results with expression of known marker genes to define hematopoietic cell populations.

LARRY barcode calling

We performed LARRY barcode retrieval from the same scRNA-seq data using a custom pipeline adapted from the LARRY framework (Rodriguez-Fraticelli et al., 2020). From paired-end 10× sequencing data, Read 2 (R2) contained the LARRY barcode insert. We extracted lineage barcode sequences using a regular expression matching the fixed flanking regions of the LARRY construct: (....)TG(....)CA(....)AC(....)GA(....)GT(....)AG(....). Read 1 (R1) provided the cell barcode (first 12 bp) and the unique molecular identifier (UMI,

next 16 bp). For each read pair, we recorded the triplet (cell barcode, UMI, lineage barcode). For each UMI (within a given cell barcode), we counted the number of supporting reads. Only UMIs supported by ≥10 reads were retained as high-confidence UMIs. This step removed potential PCR duplicates or sequencing errors. Only (cell barcode, lineage barcode) pairs supported by ≥5 distinct UMIs were considered reliable. To correct for base-calling errors or lentiviral recombination, we merged lineage barcodes within a Hamming distance of 4. After Hamming-distance merging, a given cell could still possess multiple distinct representative barcodes (due to double infection or multiple integration events). In such cases, we merged all representative barcodes for that cell into a single composite barcode by concatenating them with underscores. This composite barcode served as the unique clonal identifier for that cell. Cells with no valid (cell barcode, lineage barcode) pair passing the above filters were excluded from clonal analysis. All cells sharing the same lineage barcode were defined as members of the same clone. Only clones containing at least three cells were retained for downstream analysis.

Clone subtyping

For each clone derived from a recipient mouse, we quantified its lineage output contribution to three broad lineages: granulocyte/monocyte (GM), megakaryocyte/erythroid (ME), and lymphoid (Ly). For a given clone, the proportion of cells belonging to each lineage was normalized so that the three proportions summed to 1 (i.e., GM+ME+Ly=1). This normalized lineage distribution profile was used as the input for clustering. To classify clones by their lineage output bias, we performed *k*-means clustering combined with principal component analysis (PCA) using a clustergram approach, as previously described (Benz et al., 2012). Briefly, for each *k* in a range of 2 to 8, we ran *k*-means clustering on the normalized lineage profiles (20 random starts, maximum 100 000 iterations). The first principal component of the data was calculated using PCA. For each value of *k*, we projected the cluster centers onto the first principal component, and each individual clone was assigned a "noise" value (based on its within-cluster order) to avoid overlapping points. The resulting clustergram plots the PCA-weighted mean of each cluster against the number of clusters *k*, with lines colored by clone identity. The optimal number of clusters was determined by visual inspection of the clustergram and the stability of cluster assignments across *k* values. This analysis consistently supported three distinct clonal subtypes.

The three subtypes were named based on their lineage bias: balanced clones (roughly equal contribution across GM, ME, and Ly), Myeloid-biased (My-biased) clones (predominant contribution to GM and ME with low lymphoid output), and Lymphoid-biased (Ly-biased) clones (dominant lymphoid contribution). For visualization, each clone was plotted on a ternary plot where the three vertices represent GM, ME, and Ly lineages, and the position of each clone reflects its normalized lineage distribution.

Transcriptional persistence along differentiation trajectory

To assess whether transcriptional persistence is stably maintained or progressively lost during differentiation, we performed pseudotime trajectory inference using Slingshot (v.2.20.0) (Street et al., 2018). We used the UMAP coordinates as the reduced-dimensional space and the annotated clusters in Figure 1 as the cluster labels. We specified the HSC cluster as the starting point and allowed Slingshot to identify all possible differentiation trajectories from HSCs to six mature lineages: megakaryocyte (Mk), erythroid (Ery), basophil (Bas), neutrophil (Neu), monocyte/macrophage (Mono/Mac), and T/NK cells.

To quantify transcriptional persistence, we defined subtype-specific gene sets that capture the core transcriptional features stably retained across differentiation. For each subtype (balanced and My-biased), we selected genes that were upregulated in HSCs and maintained consistent upregulation in the same subtype in at least three of six additional hematopoietic populations. Module scores of these gene sets were then calculated for each cell using the AddModuleScore function in Seurat.

For each lineage-specific trajectory, we extracted the pseudotime values for cells assigned to that lineage and tracked the expression dynamics of the persistence gene sets along the pseudotime. Visualization of the trajectories was performed using the built-in Slingshot plotting functions.

Clonal output activity and lineage bias definition

For each HSC clone (clones containing at least one HSC), we quantified two key functional properties (output activity and lineage bias) following the established definitions from a previous study (Rodriguez-Fraticelli et al., 2020).

Output activity: To capture each clone's balance between self-renewal and differentiation, we calculated output activity A_i for clone i. Let H_i be the number of cells assigned to the HSC cluster, and K_i the number of non-HSC cells. The relative frequency of clone i in the HSC and non-HSC compartments across all clones is first computed as:

$$h_i = \frac{H_i}{\sum_j H_j}, \quad k_i = \frac{K_i}{\sum_j K_j} \tag{1}$$

Output activity is then defined as:

$$A_i = \frac{k_i}{h_i + \varepsilon} \tag{2}$$

where ε=0.0001 is a small pseudocount added to avoid division by zero. A_i thus represents the ratio of differentiation (non-HSC contribution) to self-renewal (HSC contribution) for a given clone.

For each clone, we generated a null distribution of output activity using 1 000 permutations. We randomly sampled 10% of all HSC cells (without replacement) and combined them with all non-HSC cells. From this mixed set, we recomputed the output activity A_i for the clone. Separately, we randomly sampled 10% of all non-HSC cells and combined them with all HSC cells, then recomputed A_i. This procedure yielded two paired sets of 1 000 permuted A_i values for each clone. The two distributions were compared using a two-sided Welch's *t*-test. The resulting *P*-value indicates whether the clone's output activity is significantly different from the null expectation. All *P*-values from the permutation tests were adjusted for multiple comparisons using the Benjamini-Hochberg false discovery rate procedure. A *P*-adjust<0.05 was considered statistically significant. A clone was classified as high-output if its observed A_i fell significantly above the null and as low-output if significantly below. Clones with *P*-adjust≥ 0.05 were considered to have neutral output activity.

Lineage bias: For a specific differentiated lineage L (e.g., megakaryocyte, granulocyte/monocyte, erythroid, or lymphoid), we computed a bias score $B_{i,L}$ as:

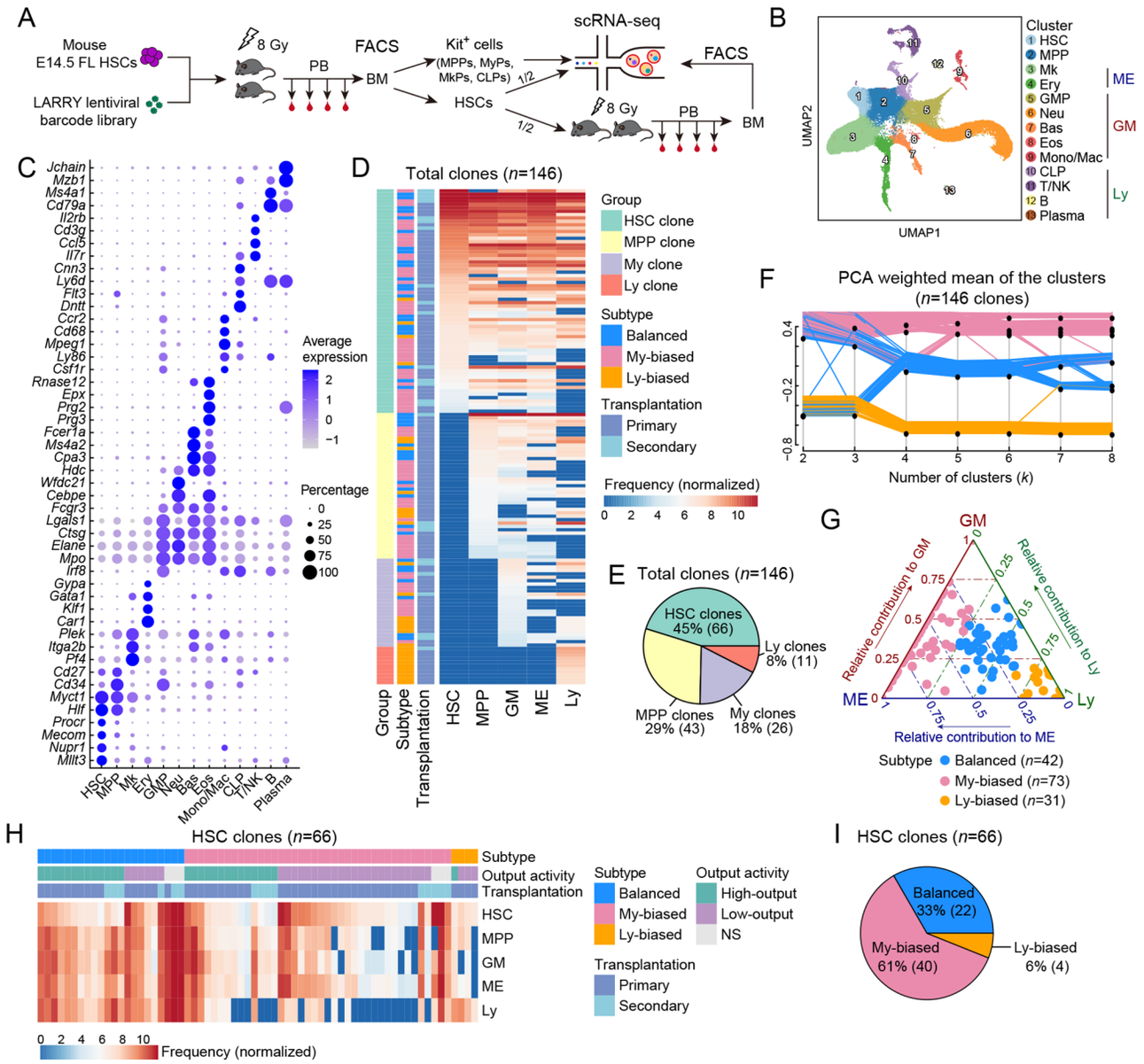

Figure 1 Simultaneous single-cell lineage and transcriptome sequencing reveals functional heterogeneity of fetal liver HSCs

A: Experimental workflow for profiling fetal liver hematopoietic stem cell (HSC) heterogeneity using the LARRY lentiviral barcoding library. E14.5 mouse fetal liver (FL) ESLAM-HSCs ($CD45^+CD201^+CD48^-CD150^+$) were transduced ex vivo and transplanted into lethally irradiated primary recipients. Long-term reconstitution was assessed in peripheral blood (PB) and bone marrow (BM), followed by fluorescence-activated cell sorting (FACS) and single-cell RNA sequencing (scRNA-seq). Half of the sorted HSCs were used for transcriptomic and clonal analysis; the other half were transplanted into secondary recipients to evaluate self-renewal. All sorted cells were used for transcriptomic and clonal analysis for secondary recipients. MPPs, multipotent progenitors; MkPs, megakaryocyte progenitors; MyPs, myeloid progenitors; CLPs, common lymphoid progenitors. B: UMAP visualization of 57 017 high-quality single cells from recipient bone marrow, colored by 13 distinct hematopoietic populations identified through unsupervised clustering. Mk, megakaryocyte; Ery, erythroid; GMP, granulocyte-monocyte progenitor; Neu, neutrophil; Bas, basophil; Eos, eosinophil; Mono/Mac, monocyte/macrophage; T/NK, T cell/NK cell; B, B cell. C: Feature plots showing expression of selected marker genes for identification of distinct hematopoietic cell populations. D: Heatmap showing normalized barcode frequencies across lineages for all 146 quality-controlled clones (size ≥3 cells). Clone groups: HSC clones (contain HSCs), MPP clones (contain MPPs but no HSCs), My clones (no HSCs or MPPs; only myeloid/megakaryocyte/erythroid cells), and Ly clones (only lymphoid cells). E: Pie chart of clone groups, as defined in D. F: *k*-means clustering of lineage contribution profiles for all 146 clones (clone size ≥3 cells) visualized by principal component analysis (PCA) values. Lines indicate three distinct clonal subtypes. G: Ternary plot depicting each clone's relative contributions to granulocyte/monocyte (GM), megakaryocyte/erythroid (ME), and lymphoid (Ly) lineages. Each dot represents a clone, colored by the corresponding subtype identified in D. Clones are colored by subtype from D: Myeloid-biased (My-biased, enriched for GM/ME), lymphoid-biased (Ly-biased, enriched for Ly), and balanced (equitable contribution across lineages). H: Heatmap showing normalized barcode frequencies in indicated lineages for the 66 HSC clones (≥1 cell in HSC cluster). Clones are grouped by subtype. NS, not significant. I: Pie chart of clone subtypes, as defined in H.

$$B_{i,L} = \frac{k_{i,L}}{k_{i,\text{non-L}} + \varepsilon} \quad (3)$$

Where $k_{i,L}$ is the number of cells of clone that belong to lineage L (within the non-HSC compartment), and $k_{i,non-L}$ is the

number of non-HSC cells of clone i that do not belong to lineage L. This metric quantifies the relative enrichment of a given lineage within the differentiated progeny of a clone.

The same permutation framework was applied to lineage bias scores. For each lineage L (GM, Mk, Ery, Ly), we performed 1 000 permutations. In each permutation, we randomly sampled 10% of cells belonging to the target lineage L (within the non-HSC compartment) and combined them with all non-HSC cells not belonging to L, then recomputed $B_{i,L}$. We randomly sampled 10% of non-HSC cells not belonging to L and combined them with all non-HSC cells belonging to L, then recomputed $B_{i,L}$. The two sets of 1 000 permuted bias values were compared using a two-sided Welch's *t*-test. All *P*-values from the permutation tests were adjusted for multiple comparisons using the Benjamini-Hochberg false discovery rate procedure. A *P*-adjust<0.05 indicated that the clone exhibits a statistically significant bias toward (or away from) the given lineage.

Detailed output activity and lineage bias values for each HSC clone are provided in Supplementary Table S2.

Differentially expressed gene identification and enrichment analysis

Differentially expressed genes (DEGs) were determined using the FindAllMarkers function in Seurat. A Wilcoxon rank-sum test was applied to compare gene expression between a given cluster and others. Only genes expressed in at least 10% of cells within the cluster were considered. DEGs were defined as those with an absolute fold change >1.5 and a *P*-adjust<0.05 from the Wilcoxon test. For comparisons involving low-output vs. high-output clonal subtypes (in both the present fetal liver dataset and the published bone marrow dataset (Rodriguez-Fraticelli et al., 2020), as well as Mk-biased vs. Multilineage subtypes in the bone marrow data, a raw *P*-value<0.01 was used to enhance sensitivity for detecting biologically relevant signals.

Gene Ontology (GO) enrichment analysis was performed using ClusterProfiler (v.4.0.5) on the identified marker genes for each cluster. The hypergeometric test was used to assess over-representation of GO terms (Biological Processes). The resulting *P*-values were adjusted for multiple comparisons using the false discovery rate (FDR) method. GO terms with a *P*-adjust<0.05 were considered significantly enriched and were retained for interpretation. To perform multi-group enrichment analysis, we utilized Metascape (http://metascape.org).

Gene signature scores

Selected gene sets, such as the stemness signatures (Giladi et al., 2018; Pei et al., 2020; Pietras et al., 2015) and selected biological processes, were scored using the AddModuleScore function in Seurat with default parameters.

Statistical analysis

All statistical analyses were conducted in R. A two-sample Wilcoxon rank-sum test was employed for comparisons of transcript counts, gene expression levels, and feature scores between two given clusters of cells.

RESULTS

Balanced and myeloid-biased HSC clones predominate in the mouse fetal liver

To simultaneously capture mRNA and lineage information from individual HSC clones, we employed a lentiviral LARRY barcode library in conjunction with scRNA-seq. To assess whether the LARRY library could effectively transduce fetal liver HSCs ex vivo, we sorted E14.5 fetal liver ESLAM-HSCs ($CD45^+CD201^+CD48^-CD150^+$; Supplementary Figure S1A), infected them for 8 h, and cultured them for 72 h after medium replacement. Subsequent FACS analysis revealed that nearly 30% of the HSCs were GFP^+, confirming robust transduction by the library (Supplementary Figure S1B). We then labeled E14.5 fetal liver ESLAM-HSCs with the validated barcode library (Figure 1A). We chose to barcode HSCs from fetal liver at the E14.5 stage because this stage provides a sufficient number of HSCs (Bowie et al., 2006; Ema & Nakauchi, 2000) and precedes the onset of HSC migration to the bone marrow (Hall et al., 2022). Given that the LARRY library contains about 2.5×10^5 unique barcodes in terms of diversity, to ensure less than 1% barcode overlap between clones (Weinreb et al., 2020), about 2 500 ESLAM-HSCs were co-cultured with the barcode library and subsequently transplanted into lethally irradiated recipient mice. Longitudinal analysis of peripheral blood confirmed GFP^+ donor contribution across five lineages (Supplementary Figure S1C–E, *n*=10 primary transplantation recipients). More than 16 weeks after transplantation, confirming long-term reconstitution, GFP^+ hematopoietic stem and progenitor cells (HSPCs), including purified HSCs, MPPs, MkPs, MyPs (Sawai et al., 2016), and CLPs, were sorted from the bone marrow of primary recipients (Supplementary Figure S1F; Supplementary Table S1). Half of the sorted cells were processed for 10× Genomics scRNA-seq, while HSCs from the other half were injected into secondary recipients to assess self-renewal potential. Through regular monthly detection of peripheral blood, multilineage reconstitution was detected by flow cytometry after 16 weeks of transplantation, with an overall chimerism rate (GFP^+) of 48.53±5.71% (mean±SEM) (Supplementary Figure S1G, H; *n*=8 secondary transplantation recipients). Likewise, GFP^+ HSPC populations were sorted from the bone marrow of secondary recipients and subjected to scRNA-seq. In total, five recipient mice from the primary recipients and five from the secondary recipients were selected for scRNA-seq (Supplementary Table S1).

After stringent quality control, we obtained 57 017 high-quality single cells, with a barcode detection rate of 70.57±6.30% (mean±SEM) (Supplementary Figure S2A). Unsupervised clustering followed by marker gene annotation delineated 13 transcriptionally distinct hematopoietic populations (Figure 1B, C). Although our sorting strategy targeted progenitor cells, we still captured a small number of mature lineage cells, consistent with previous single-cell studies that employed similar isolation strategies (Supplementary Figure S2B) (Hall et al., 2022; Rodriguez-Fraticelli et al., 2020). The HSC cluster was distinguished by elevated expression of stemness-associated genes, including *Hlf*, *Procr*, *Mecom*, and *Mllt3* (Figure 1C). All 13 populations were detected in each recipient mouse, and all captured valid barcodes (65.07±5.47% per population, mean±SEM) (Supplementary Figure S2C, D). After applying a clonal threshold of ≥3 cells per barcode, we identified 146 clones spanning the entire hematopoietic hierarchy, and these clones could be classified into four groups according to their population contribution: HSC clones, MPP clones, My clones, and lymphoid (Ly) clones (Figure 1D, E).

To classify these clones by lineage output, we performed *k*-means clustering on the lineage distribution profiles of all 146

clones, which revealed three distinct clusters (Figure 1F; see Materials and methods). Projecting these clones onto a ternary plot defined by the three principal lineage dimensions (lymphoid, myeloid, and megakaryocytic/erythroid) showed a clear separation that corresponded to the three clusters (Figure 1G). Accordingly, we designated the three clusters as balanced, myeloid-biased (My-biased), and lymphoid-biased (Ly-biased) subtypes. We then focused on the 66 clones that contained HSCs (i.e., clones with at least one cell assigned to the HSC cluster) (Figure 1E). Heatmap visualization of their lineage contributions showed that balanced (22 clones, 33%) and My-biased (40 clones, 61%) clones were abundant, whereas Ly-biased clones (4 clones, 6%) were rare (Figure 1H, I; Supplementary Table S2).

Secondary transplantation is the gold standard for identifying long-term self-renewing HSCs. We therefore examined barcode sharing between primary and secondary recipients. Among the 66 HSC clones, 48 had been tracked in both primary and secondary transplantation experiments, thus permitting assessment of durable self-renewal capacity. Of these, 75% were detected only in primary recipients and thus lacked durable self-renewal capacity; 20% were shared between primary and secondary recipients, representing long-term reconstituting HSCs; and 5% appeared exclusively in secondary recipients, suggestive of dormant HSC clones that were not activated in primary recipients (Supplementary Figure S2E). However, we acknowledge that stochastic or technical factors, such as extremely low-level contribution in the primary recipient below detection limits, cannot be formally excluded.

Among the clones with long-term reconstitution capacity, which accounted for 20% of all HSC clones (Supplementary Figure S2E), only balanced and My-biased HSC subtypes were present, and their clone numbers were 6 and 2, respectively (Supplementary Figure S2F). These numbers were not significantly different from the overall clonal distribution of 40 and 22 (P=0.1974) (Figure 1I), indicating that durable long-term clones do not preferentially belong to either subtype. It has been reported that My-biased and balanced HSC clones in adult bone marrow can interconvert upon serial transplantation (Benz et al., 2012; Dykstra et al., 2007; Fukushima et al., 2025). We found that, in the fetal liver, about 62.5% of HSC clones (5/8) maintained their lineage bias identity throughout the transplantation period, whereas a minority (3/8, 37.5%) tended to shift between My-biased and balanced subtypes (Supplementary Figure S2F). However, given the limited clone numbers, these observations remain preliminary. Future studies will require larger clone cohorts and the introduction of new barcodes into the secondary transplant HSCs to further track subclone dynamics.

We next compared the transcriptomic profiles between long-term (detected in both primary and secondary recipients) and short-term (detected only in primary recipients) HSC clones. Long-term HSC clones showed relatively higher expression of *Hes1*, *Nr4a1*, *H3f3b*, and *Apoe*, whereas short-term HSC clones showed relatively higher expression of myeloid-associated inflammatory genes including *Prss34*, *Camp*, *S100a9*, and *S100a8* (Supplementary Figure S2G). GO enrichment analysis further showed that long-term HSC clones were enriched in regulation of inflammatory response, cell proliferation, and cell differentiation, whereas short-term HSC clones were enriched in leukocyte aggregation, DNA replication, and DNA repair-related processes (Supplementary Figure S2H).

Balanced and My-biased HSC clones display markedly distinct transcriptomes

Fetal liver HSCs included several exceptionally large clones distributed among the balanced and My-biased subtypes. Within the HSC population, the largest clone, belonging to the balanced subtype, contained 901 HSCs (Figure 2A). The median clone size of HSCs in the balanced subtype was significantly greater than that in the My-biased subtypes (P<0.05), suggesting a higher expansion rate of balanced HSC clones (Figure 2B). This is consistent with earlier single-cell transplantation findings showing that balanced β-HSCs possess the highest expansion capacity among fetal liver HSC subtypes (Benz et al., 2012). Stemness gene set scoring further revealed that balanced HSC clones displayed significantly more pronounced stemness characteristics (Giladi et al., 2018; Pei et al., 2020; Pietras et al., 2015) than My-biased clones (Figure 2C), with relatively higher expression of canonical stemness genes such as *Hlf*, *Mllt3*, and *Kit* (Figure 2D).

Gene Set Enrichment Analysis (GSEA) and GO enrichment analyses uncovered fundamentally distinct transcriptional programs underlying these two clonal subtypes (Figure 2E, F). The My-biased HSC subtype highly expressed gene sets related to cell cycle progression (e.g., E2F targets, Myc targets, G2/M checkpoint), DNA repair, and energy metabolism (e.g., oxidative phosphorylation, fatty acid metabolism), indicative of a highly proliferative and metabolically active state. The balanced HSC subtype, by contrast, was enriched for gene sets associated with lymphoid differentiation, hypoxia response, and multiple inflammatory and stress signaling pathways (e.g., IFN-γ, TGF-β, TNF, and MAPK signaling). These inflammatory pathways, particularly IFN signaling, have been implicated in regulating HSC maturation during embryonic development and in modulating HSC maintenance, activation, and lineage commitment in the bone marrow (Arora et al., 2014; Kim et al., 2016). Of note, the larger clone size of the balanced HSC subtype did not correlate with higher cell-cycle transcriptional activity at the time of analysis (Figure 2B, E). This apparent dissociation between clone size and current cycling status suggests a distinction in expansion history that warrants further investigation. Together, these results reveal significant differences in stemness and transcriptomic signatures between balanced and My-biased HSC subtypes.

Transcriptomic signatures of lineage-biased HSC subtypes are stably retained in progeny

To robustly assess whether the transcriptional differences between balanced and My-biased HSC subtypes are preserved during differentiation, we focused on hematopoietic populations with more than 200 cells in each subtype, ensuring sufficient statistical power and representativeness (Figure 2G). Differential expression analysis comparing the same population across the two subtypes revealed that balanced HSCs and their progeny consistently expressed significantly higher levels of genes such as *Rpl34*, *Tjp1*, and *Hist1h2ao*, whereas My-biased HSCs and their progeny consistently upregulated *Prss34*, *Psma8*, and *Mcpt8* (Figure 2H). To further examine the consistency of these transcriptional signatures across cell types and clonal subtypes, we visualized the overlap among upregulated gene lists using a circos plot (Figure 2I). Strikingly, extensive gene-

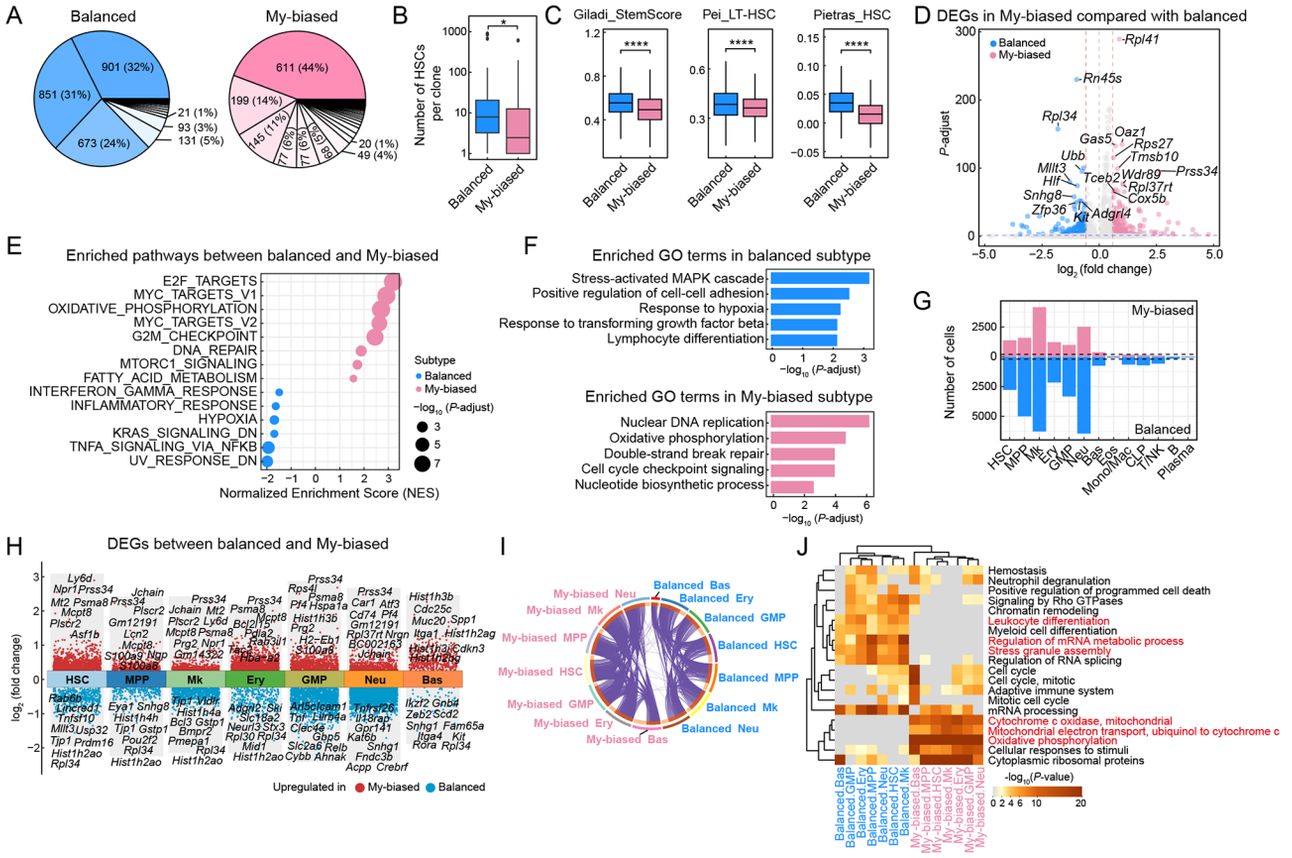

Figure 2 Balanced and My-biased HSC subtypes display distinct and progeny-persistent transcriptomic programs

A: Pie charts illustrating the absolute number and proportion of HSCs within balanced and My-biased subtypes. B: Box plot showing a significantly higher number of HSCs per clone in balanced compared to My-biased HSC subtypes. *: P<0.05. C: Box plot showing significantly higher stemness gene set scores in balanced compared to My-biased subtypes. ****: P<0.0001. D: Volcano plot of differentially expressed genes (DEGs; P-adjust<0.05 and fold change >1.5) between balanced and My-biased subtypes. Selected up- and down-regulated genes are labeled. E: Gene Set Enrichment Analysis (GSEA) identifies significantly enriched signaling pathways between the balanced and My-biased subtypes. F: GO enrichment analysis reveals the significantly enriched biological processes between the balanced and My-biased subtypes. G: Bar plots quantifying cell numbers of distinct hematopoietic populations derived from balanced and My-biased subtypes. Only populations with >200 cells per subtype (dashed lines) are used for downstream analysis. H: Volcano plots of upregulated DEGs comparing the same cell population between balanced and My-biased subtypes. Selected upregulated DEGs are labeled. I: Circos plot illustrating the gene overlap of the top 200 upregulated DEGs across distinct cell populations within balanced and My-biased subtypes. The inner circle represents gene lists, where hits are arranged along the arc. Genes that hit multiple lists are colored in dark orange, and genes unique to a list are shown in light orange. The limited cross-subtype connectivity underscores the stable retention of these transcriptional programs, termed “transcriptional persistence”. J: Metascape analysis of biological processes enriched in the upregulated DEGs shown in H.

level overlap was observed among different cell populations within the same subtype, whereas very few connections were detected between subtypes. GO enrichment analysis further demonstrated that cell populations of the balanced subtype were consistently enriched for biological processes including leukocyte differentiation, regulation of mRNA metabolic process, and stress granule assembly, whereas cell populations of the My-biased subtype were consistently enriched for metabolic processes such as cytochrome c oxidase activity, mitochondrial electron transport, and oxidative phosphorylation (Figure 2J; Supplementary Figure S3A). Together, these results underscored the distinct transcriptional programs of the two subtypes and demonstrated that these programs were stably retained across multiple hematopoietic lineages. We term this phenomenon “transcriptional persistence”.

To determine whether transcriptional persistence is maintained or progressively lost during differentiation, we performed pseudo-temporal trajectory analyses from HSCs to six lineages: megakaryocyte, erythroid, basophil, neutrophil, monocyte/macrophage, and T/NK cells (Supplementary Figure S3B). We defined two core transcription persistence gene sets, one for balanced clones and one for My-biased clones, as those consistently upregulated within each subtype across HSCs and at least three downstream populations (Figure 2H). Tracking the expression dynamics of these gene sets along each lineage-specific pseudotime trajectory revealed that the subtype-specific transcriptional signatures remained largely stable across most differentiation trajectories, without progressive decline (Supplementary Figure S3C, D). However, in certain lineages, particularly erythroid, the transcriptional differences between balanced and My-biased clones diminished at the terminal stage, suggesting that persistence maintenance may be lineage-context dependent.

To further explore the relationship between transcriptional persistence and lineage bias, we examined clones that underwent lineage bias switching during serial transplantation. Notably, when lineage bias changed, the transcriptional

persistence signatures shifted correspondingly, as reflected by changes in subtype-specific gene set scores (Supplementary Figure S3E–G). This indicates that persistence is not fixed to the initial HSC state but can dynamically shift with alterations in lineage bias.

Notably, applying the same analytical framework to adult bone marrow HSCs (Rodriguez-Fraticelli et al., 2020) did not reveal transcriptional persistence (Supplementary Figure S3H, I).

Fetal liver HSCs with different output activities exhibit distinct transcriptomic features

We next evaluated the progeny output activity of each HSC clone (Supplementary Table S2), a metric previously used to classify adult bone marrow HSC clones (Rodriguez-Fraticelli et al., 2020). For each clone, output activity was quantified as the normalized ratio of non-HSC progeny to HSC cells, based on which output activity values and the low-output and high-output HSC clones were identified (see Materials and methods). Fisher's exact test revealed no significant association between output activity and lineage bias (P=0.1487), indicating that these two dimensions represent largely independent axes of fetal liver HSC heterogeneity (Supplementary Figure S4A).

Consistent with observations in adult bone marrow, fetal liver HSC frequency was negatively correlated with output activity and positively correlated with progeny frequency (Figure 3A). While about 25% of adult bone marrow HSC clones have been reported to exist in a "differentiation-inactive" state (i.e., clones without any lineage output) (Pei et al., 2020; Rodriguez-Fraticelli et al., 2020), we did not detect any such clones in the fetal liver (Figure 3A). Consequently, the fetal liver displayed a distinct distribution of clonal output activity compared with adult bone marrow (Figure 3B). However, our clone cohort (n=66) would have limited power to detect such clones if they existed at a frequency below approximately 4%.

In adult bone marrow, low-output HSCs are known to exhibit stronger stemness programs than high-output HSCs, and only low-output clones possess durable long-term reconstitution capacity (Rodriguez-Fraticelli et al., 2020). In contrast, fetal liver low-output and high-output HSCs displayed comparable stemness gene set scores (Giladi et al., 2018; Pei et al., 2020;

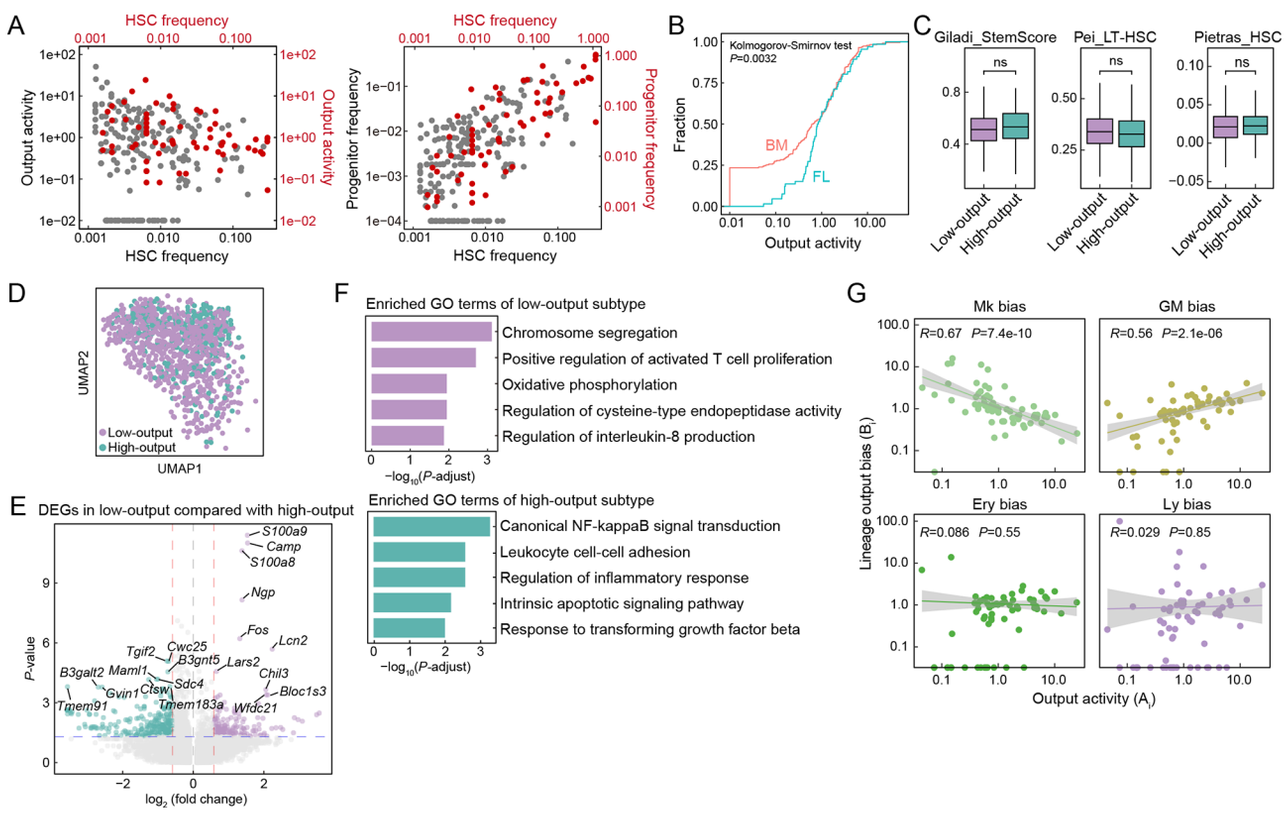

Figure 3 Fetal liver HSCs with different output activities have distinct transcriptomic features

A: Scatter plots depicting the relationship between HSC frequency (proportion of clone cells residing in the HSC compartment) and progeny output activity (normalized ratio of non-HSC to HSC cells, left panel) (Spearman correlation coefficient, –0.25), as well as between HSC frequency and progenitor frequency (proportion of clone cells in the non-HSC compartment, right panel) (Spearman correlation coefficient, 0.78). Red dots represent clones identified in this study (fetal liver), while gray dots are reproduced from adult bone marrow data for comparison. B: Cumulative distribution curves comparing the output activity of HSC clones between fetal liver (FL, this study) and adult bone marrow (BM, reproduced data). A two-sample Kolmogorov-Smirnov test reveals a significant difference between the two distributions (P=0.0032). C: Box plots showing no significant difference in stemness gene set scores between low-output and high-output HSC clones. ns: not significant. D: UMAP projection of HSCs colored by clonal output activity (i.e., low-output and high-output). E: Volcano plot of DEGs between low-output and high-output clonal subtypes using a more liberal threshold (P-value<0.05 and fold change >1.5) to prioritize sensitivity. Selected up- and down-regulated genes are labeled. F: GO enrichment analysis reveals the significantly enriched biological processes in DEGs between the low-output and high-output clonal subtypes. G: Scatter plots correlating lineage bias scores (Mk, GM, Ery, Ly) with output activity. GM bias shows a significant positive correlation, while Mk bias is negatively correlated with output activity, consistent with adult bone marrow patterns.

Pietras et al., 2015) (Figure 3C). Their distribution on the UMAP was also well intermingled (Figure 3D), contrasting sharply with the distinct hierarchical relationship observed in adult bone marrow HSCs (Rodriguez-Fraticelli et al., 2020). Moreover, low-output and high-output fetal liver HSCs contributed durable long-term clones, with counts of 5 and 2, respectively. These counts were not significantly different from the overall distribution of 32 and 28 (P=0.4468) (Supplementary Figure S2F).

Consistent with their indistinct transcriptional boundaries on the UMAP, very few differentially expressed genes were detected between low-output and high-output HSCs under the default stringent analytical criteria. To further resolve their potential differences, we applied more permissive thresholds and identified a number of distinguishing genes (Figure 3E). Low-output HSCs were associated with gene sets related to chromosomal segregation, positive regulation of T cell proliferation, oxidative phosphorylation, and regulation of cysteine-type endopeptidase activity (Figure 3F). High-output HSCs, by contrast, were enriched for processes related to NF-κB signaling, immune response, cell adhesion, TGF-β response, and intrinsic apoptotic signaling pathways (Figure 3F). In bone marrow (Rodriguez-Fraticelli et al., 2020), low-output clones were enriched for cell differentiation, hematopoietic regulation, and cell adhesion, whereas high-output clones were enriched for cell migration and chemotaxis pathways (Supplementary Figure S4B), a pattern that is distinct from the fetal liver signatures described above.

To further characterize lineage bias at finer resolution, we computed for each HSC clone a bias score toward the Mk, GM, Ery, and Ly lineages, defined as the normalized ratio of cells of the given lineage to other non-HSC cells (see Materials and methods). We then examined the relationship between these lineage bias scores and output activity. Consistent with the pattern reported in adult bone marrow, the Mk bias score was negatively correlated with output activity. Additionally, we found that the GM bias score showed a significant positive correlation, and erythroid and lymphoid bias scores displayed no significant correlation with output activity (Figure 3G; Supplementary Figure S4C, D).

Importantly, across both fetal liver and adult bone marrow HSCs, we found no evidence of transcriptional persistence when comparing subtypes defined by output activity (Supplementary Figure S4E, F), suggesting a specific coupling relationship between transcriptional persistence and lineage bias.

Molecular subsets of fetal liver HSCs are partially coupled to lineage output bias

To explore the molecular heterogeneity of fetal liver HSCs, we performed subclustering of the HSC population (4 705 cells) and identified two transcriptionally distinct subsets, termed Mllt3_HSC and Cd34_HSC (Figure 4A). Mllt3_HSC was characterized by elevated expression of genes such as *Mllt3*, *Cd74*, and *Hes1*, along with prominent stemness scores (Figure 4B, C). In contrast, Cd34_HSC exhibited high expression of *Cd34*, *Stmn1*, *Slc22a3*, *H2afz*, and *H2afy* (Figure 4B), genes that have also been reported as signature genes of high-output and multilineage HSCs from adult bone marrow (Rodriguez-Fraticelli et al., 2020). GO enrichment analysis revealed that Mllt3_HSC was enriched for type II interferon response, IFN-β response, and lymphoid/myeloid cell differentiation, whereas Cd34_HSC was enriched for DNA replication, cell cycle transition, and cell cycle regulation (Figure 4D), suggesting that Cd34_HSC represents a more active cycling state.

We next examined the relationship between these molecular subsets and the functionally defined clonal subtypes. When the clonal subtypes were projected onto the UMAP of the HSC population, the balanced HSC subtype was relatively concentrated in the Mllt3_HSC region, while the My-biased HSC subtype was more evenly distributed across both Mllt3_HSC and Cd34_HSC regions (Figure 4E). Proportional analysis confirmed that Mllt3_HSC was more abundant in balanced than My-biased HSC subtype (P<0.0001), and Cd34_HSC was enriched in My-biased HSC subtype (P<0.0001) (Figure 4F). At the clonal level, we observed a trend towards a higher Mllt3_HSC/Cd34_HSC ratio in the balanced subtype compared with the My-biased subtype, albeit with no statistical significance (P=0.13) (Figure 4G; considering clones with ≥10 HSCs). These results suggest that transcriptomic features alone can partially correlate with lineage output bias at the population level. However, the lack of statistical significance at the clonal level indicates that the predictive power of these molecular subsets is limited. In the future, integrating multi-omics data such as epigenomic and metabolomic profiles may improve the accuracy of molecular feature-based prediction of lineage output identity.

DISCUSSION

In this study, we combined lentiviral barcode tracing with single-cell transcriptomics to systematically dissect, for the first time at clonal resolution, the functional heterogeneity of mouse E14.5 fetal liver HSCs. We identified three clonal subtypes defined by lineage output bias: balanced, myeloid-biased, and lymphoid-biased. The overall composition of these subtypes differed markedly from the report by the Eaves group (Benz et al., 2012), with the most pronounced difference being the representation of lymphoid-biased clones. In our study, lymphoid-biased clones constituted only 6% (95% confidence interval: 2%–15%) of the total, whereas in the previous work they accounted for nearly half of all clones. We view this difference not as a contradiction, but as a reflection of several methodological and contextual factors that likely overrepresent lymphoid-biased clones in the previous study. First, the definition of lineage bias subtypes was based on bone marrow output of GM, ME, and Ly lineages in this study, whereas it was based on peripheral blood GM, B, and T lineages in the previous study (Benz et al., 2012). Second, our analysis was restricted to clones containing HSCs in recipient bone marrow, whereas the classification method used in previous studies did not distinguish whether clones contained HSCs (Benz et al., 2012). For instance, given the long lifespan of lymphoid cells, this could overestimate the frequency of lymphoid-biased clones. Third, our polyclonal transplantation setting introduces clonal competition and niche interactions that are absent in the single-cell transplants used previously (Benz et al., 2012). Fourth, we used wild-type recipients, whereas the previous study employed *Kit*-mutant mice, a host difference that may further influence lineage output.

Transcriptional persistence describes the stable retention of subtype-specific transcriptional programs from HSCs to their differentiated progeny. Currently, the link between transcriptional persistence and clonal subtypes remains largely correlative, leaving open the question of whether the

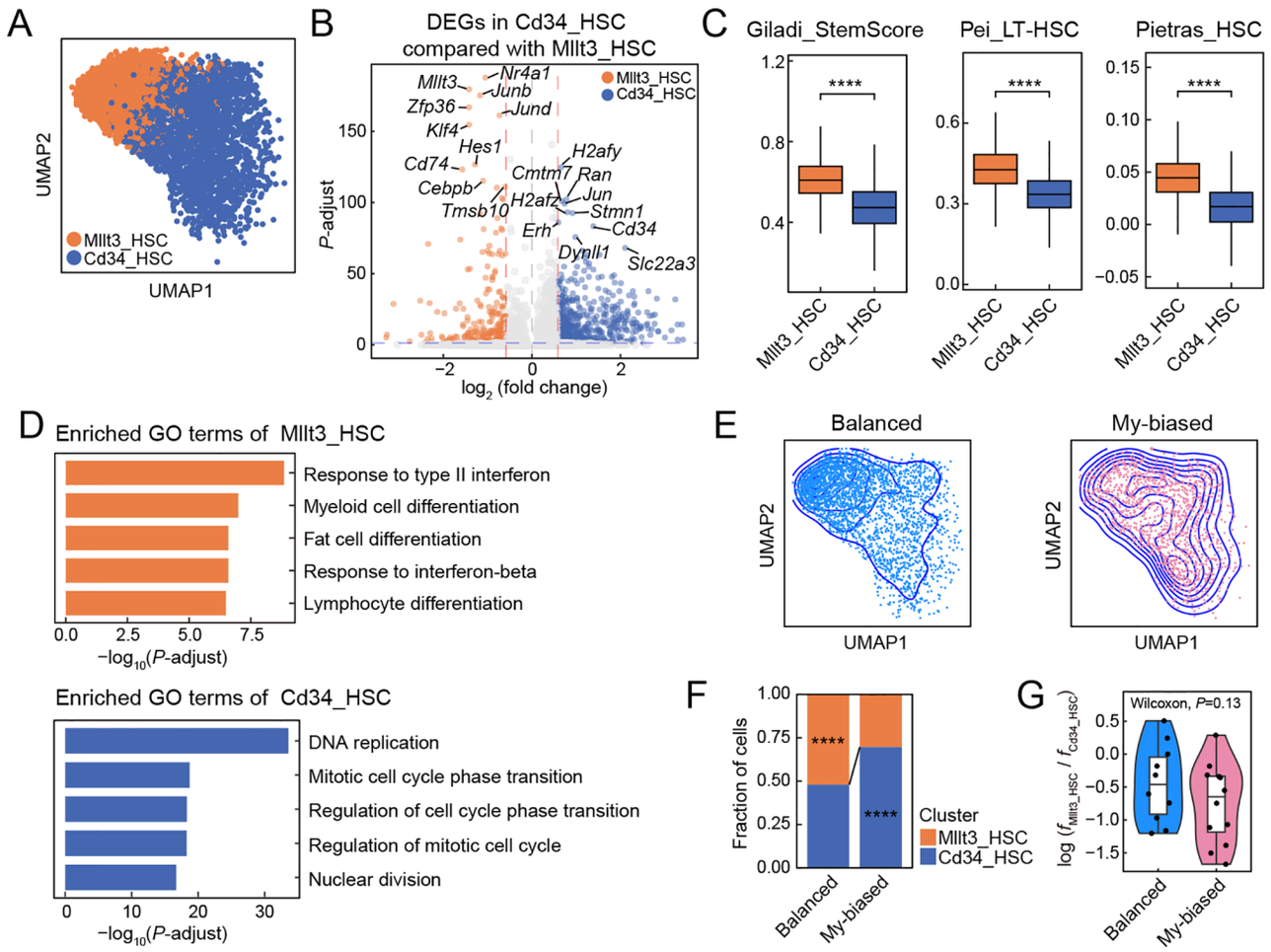

Figure 4 Molecular subsets of fetal liver HSCs are partially coupled to lineage output bias

A: UMAP plot showing two transcriptomically distinct HSC subclusters. B: Volcano plot of DEGs (*P*-adjust<0.05 and fold change >1.5) between Mllt3_HSC and Cd34_HSC subclusters. Selected up- and down-regulated genes are labeled. C: Box plots showing that Mllt3_HSC exhibits significantly higher stemness gene signature scores compared to Cd34_HSC. ****: *P*<0.0001. D: GO enrichment analysis revealing the selected 5 significantly enriched biological processes among the DEGs between Mllt3_HSC and Cd34_HSC. E: Contour plot showing the distribution of balanced and My-biased clonal subtypes over the HSC UMAP space. F: Bar chart quantifying the proportion of Mllt3_HSC vs. Cd34_HSC cells within balanced and My-biased subtypes. The balanced subtype shows a significantly higher proportion of Mllt3_HSC, and the My-biased subtype shows a higher proportion of Cd34_HSC. ****: *P*<0.0001. G: Box plot comparing the ratio of Mllt3_HSC to Cd34_HSC proportions between balanced and My-biased subtypes (Wilcoxon test, *P*=0.13).

observed persistence instructs fate, records history, or emerges from selective pressures. First, these programs may actively instruct lineage bias, for instance through embryonic transcriptional regulators that pre-configure HSCs and guide downstream fate decisions. Second, the programs might serve as passive records of clonal history, reflecting developmental origin or past lineage commitment without directly driving output. Third, the observed persistence could arise, at least in part, from transplantation-mediated selection, whereby clones with certain pre-existing expression profiles are preferentially maintained or expanded in specific lineages. Our observation that clones switching lineage bias during serial transplantation showed corresponding changes in their persistence programs (Supplementary Figure S3E–G) argues against a simple fixed instructive model. Instead, it suggests that persistence reflects current clonal identity, which can be reshaped under strong selective pressures. However, we cannot definitively distinguish whether this remodeling reflects passive recording of a new clonal state or selection acting on pre-existing heterogeneity. Future studies integrating epigenomic, proteomic, and functional perturbation approaches are needed to distinguish among the three possibilities and to elucidate the underlying mechanisms.

Notably, transcriptional persistence was not observed in adult bone marrow HSCs, nor was it correlated with progeny output activity. However, this comparison is subject to limitations including differences in developmental stage, transplantation settings, and dataset origin. Therefore, while our data suggest that transcriptional persistence may be preferentially associated with fetal liver HSCs, formal demonstration of developmental stage-specificity requires direct comparative studies under identical conditions.

In conclusion, our study provides a clonal-resolution view of fetal liver HSC heterogeneity, delineating transcriptomic differences among lineage-biased HSC subtypes and revealing that their transcriptional programs are stably retained in progeny. Furthermore, fetal liver HSCs exhibit output activity heterogeneity uncoupled from stemness (Figure 5). These two features differ significantly from those of adult bone marrow HSCs, providing a theoretical basis for understanding HSC heterogeneity across different developmental stages.

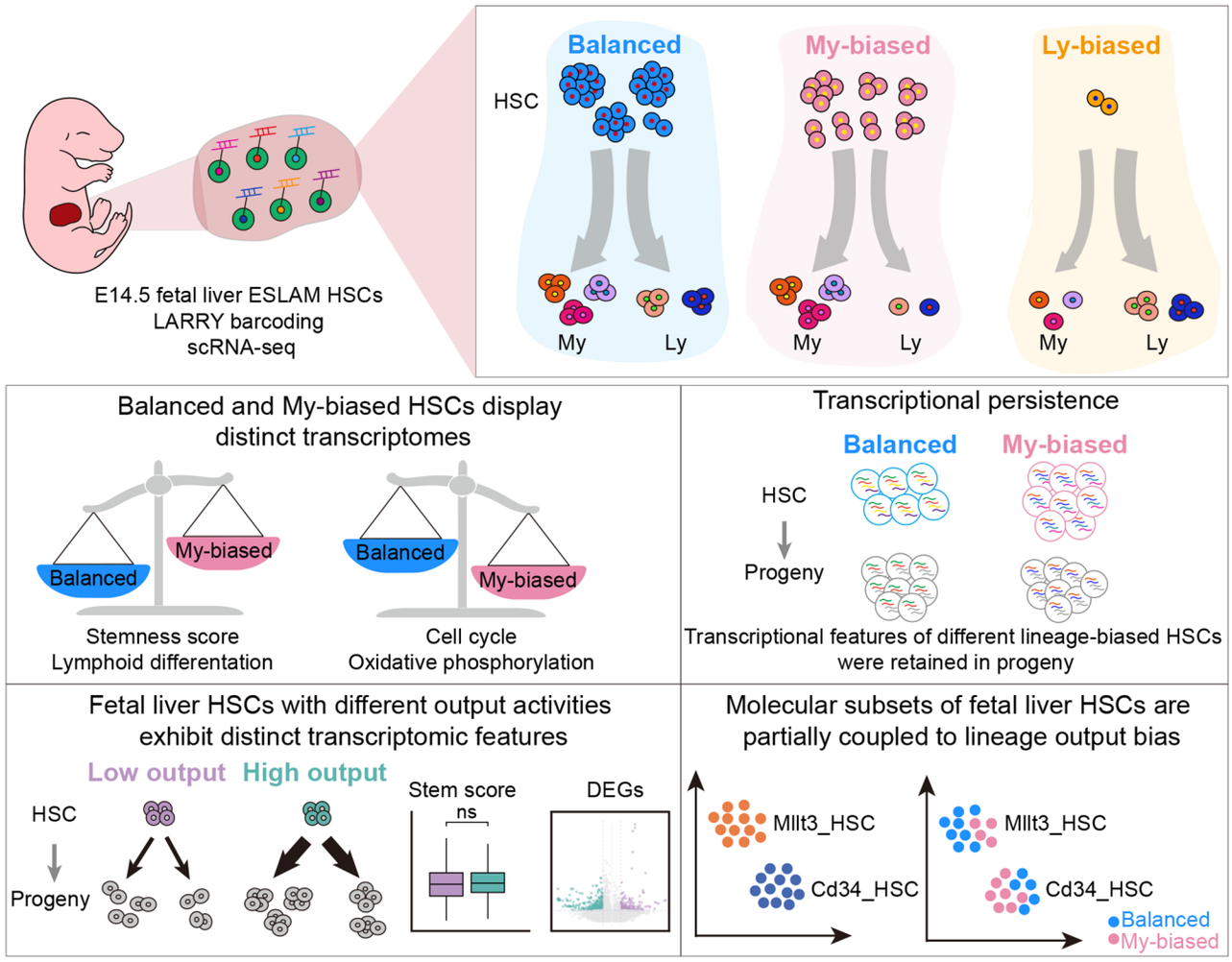

Figure 5 Summary of clonal-level functional and molecular heterogeneity of fetal liver HSCs

Three clonal subtypes (balanced, My-biased, Ly-biased) were identified, with balanced and My-biased subtypes dominating. Balanced subtypes exhibit stronger stemness and lymphoid signatures, whereas My-biased subtypes are enriched for cell cycle and oxidative phosphorylation pathways. Transcriptional features distinguishing HSC subtypes are retained in their progeny (transcriptional persistence). Output activity (low vs. high) is uncoupled from stemness in fetal liver HSCs, unlike in adult bone marrow. Despite showing no significant difference in stemness features, the two subtypes displayed distinct transcriptional profiles and signaling activation states. These characteristics also differed from those of their bone marrow counterparts. Transcriptome-based subclustering reveals that molecular subsets could potentially predict clonal lineage output bias. My: Myeloid cells; Ly: Lymphoid cells.

LIMITATIONS

Several limitations of this study should be acknowledged. First, the number of HSC clones recovered (66 clones) is modest, which limits the statistical power to detect rare subtypes and to robustly characterize clone-to-clone variation. Second, our analysis was restricted to the transcriptome, while epigenetic and proteomic features that may be integral to defining lineage bias identity were not assessed. Third, the observed "transcriptional persistence" is a correlative phenomenon. Whether it reflects a causal mechanism in lineage fate determination or simply a passive consequence of lineage bias requires functional validation, such as targeted perturbation of candidate associated genes. Fourth, our analysis focused on fetal liver HSCs following transplantation, rather than on primary HSCs. Therefore, future experiments that directly label fetal liver HSCs *in vivo* and track their clonal output from the fetal stage through to adulthood will be necessary to provide a more comprehensive view of their biological characteristics. Finally, given the differences in hematopoietic development between humans and mice (Du et al., 2021, 2024; Hou et al., 2024), whether these findings observed in mice are conserved in humans requires further investigation.

DATA AVAILABILITY

The raw sequence data generated in this study were deposited in the Genome Sequence Archive (GSA) database (https://ngdc.cncb.ac.cn/gsa/) (GSA: CRA043477), Science Data Bank (doi: 10.57760/sciencedb.38546), and NCBI (BioProjectID PRJNA1475072). The publicly available adult bone marrow LARRY clonal hematopoietic stem and progenitor cell (HSPC) single-cell data analyzed in this study were originally reported by Rodriguez-Fraticelli et al. (2020). Raw data and count matrices can be accessed at the Gene Expression Omnibus under accession GSE134242.

SUPPLEMENTARY DATA

Supplementary data to this article can be found online.

COMPETING INTERESTS

The authors declare that they have no competing interests.

AUTHORS' CONTRIBUTIONS

Z.L. and B.L. conceived and designed the study; M.Z. performed cell barcoding, culture, cell transplants, bleeding, bone marrow preparation, and data collection; Y.N. performed flow cytometry and sorting, and data collection; D.L. and D.X. performed bioinformatics analysis and data visualization; G.L., J.Z., and Y.L. advised on experimental condition exploration; M.Z. and Z.L. wrote the manuscript. All authors read and approved the final version of the manuscript.

REFERENCES

Arora N, Wenzel PL, McKinney-Freeman SL, et al. 2014. Effect of developmental stage of HSC and recipient on transplant outcomes. *Developmental Cell*, **29**(5): 621–628.

Benz C, Copley MR, Kent DG, et al. 2012. Hematopoietic stem cell subtypes expand differentially during development and display distinct lymphopoietic programs. *Cell Stem Cell*, **10**(3): 273–283.

Bowie MB, McKnight KD, Kent DG, et al. 2006. Hematopoietic stem cells proliferate until after birth and show a reversible phase-specific engraftment defect. *Journal of Clinical Investigation*, **116**(10): 2808–2816.

Bunis DG, Bronevetsky Y, Krow-Lucal E, et al. 2021. Single-cell mapping of progressive fetal-to-adult transition in human naive T cells. *Cell Reports*, **34**(1): 108573.

Cheng H, Zheng ZF, Cheng T. 2020. New paradigms on hematopoietic stem cell differentiation. *Protein & Cell*, **11**(1): 34–44.

Crisan M, Dzierzak E. 2016. The many faces of hematopoietic stem cell heterogeneity. *Development*, **143**(24): 4571–4581.

Crisan M, Kartalaei PS, Vink CS, et al. 2015. BMP signalling differentially regulates distinct haematopoietic stem cell types. *Nature Communications*, **6**(1): 8040.

Du JJ, He H, Li ZC, et al. 2021. Integrative transcriptomic analysis of developing hematopoietic stem cells in human and mouse at single-cell resolution. *Biochemical and Biophysical Research Communications*, **558**: 161–167.

Du JJ, Li ZC, Gong YD, et al. 2024. Integrative cross-species transcriptome analysis reveals earlier occurrence of myelopoiesis in pre-circulation primates compared to mice. *Zoological Research*, **45**(6): 1276–1286.

Dykstra B, Kent D, Bowie M, et al. 2007. Long-term propagation of distinct hematopoietic differentiation programs in vivo. *Cell Stem Cell*, **1**(2): 218–229.

Ema H, Morita Y, Suda T. 2014. Heterogeneity and hierarchy of hematopoietic stem cells. *Experimental Hematology*, **42**(2): 74–82. e2.

Ema H, Nakauchi H. 2000. Expansion of hematopoietic stem cells in the developing liver of a mouse embryo. *Blood*, **95**(7): 2284–2288.

Fukushima T, Kristiansen TA, Wong LP, et al. 2025. Hematopoietic stem cells undergo bidirectional fate transitions *in vivo. BioRxiv*, doi: https://doi.org/10.1101/2025.02.23.639689.

Ganuza M, Hall T, Myers J, et al. 2022. Murine foetal liver supports limited detectable expansion of life-long haematopoietic progenitors. *Nature Cell Biology*, **24**(10): 1475–1486.

Giladi A, Paul F, Herzog Y, et al. 2018. Single-cell characterization of haematopoietic progenitors and their trajectories in homeostasis and perturbed haematopoiesis. *Nature Cell Biology*, **20**(7): 836–846.

Hall TD, Kim H, Dabbah M, et al. 2022. Murine fetal bone marrow does not support functional hematopoietic stem and progenitor cells until birth. *Nature Communications*, **13**(1): 5403.

Hou SY, Guo X, Du JJ, et al. 2024. New insights into the endothelial origin of hematopoietic system inspired by "TIF" approaches. *Blood Science*, **6**(4): e00199.

Kieusseian A, De La Grange PB, Burlen-Defranoux O, et al. 2012. Immature hematopoietic stem cells undergo maturation in the fetal liver. *Development*, **139**(19): 3521–3530.

Kim PG, Canver MC, Rhee C, et al. 2016. Interferon-α signaling promotes embryonic HSC maturation. *Blood*, **128**(2): 204–216.

Kristiansen TA, Jaensson Gyllenbäck E, Zriwil A, et al. 2016. Cellular barcoding links B-1a B cell potential to a fetal hematopoietic stem cell state at the single-cell level. *Immunity*, **45**(2): 346–357.

Laurenti E, Göttgens B. 2018. From haematopoietic stem cells to complex differentiation landscapes. *Nature*, **553**(7689): 418–426.

Li YN, Kong WJ, Yang W, et al. 2020. Single-cell analysis of neonatal HSC ontogeny reveals gradual and uncoordinated transcriptional reprogramming that begins before birth. *Cell Stem Cell*, **27**(5): 732–747. e7.

Morrison SJ, Hemmati HD, Wandycz AM, et al. 1995. The purification and characterization of fetal liver hematopoietic stem cells. *Proceedings of the National Academy of Sciences of the United States of America*, **92**(22): 10302–10306.

Muller-Sieburg CE, Sieburg HB, Bernitz JM, et al. 2012. Stem cell heterogeneity: implications for aging and regenerative medicine. *Blood*, **119**(17): 3900–3907.

Pei WK, Shang FW, Wang X, et al. 2020. Resolving fates and single-cell transcriptomes of hematopoietic stem cell clones by *PolyloxExpress* barcoding. *Cell Stem Cell*, **27**(3): 383–395. e8.

Pietras EM, Reynaud D, Kang YA, et al. 2015. Functionally distinct subsets of lineage-biased multipotent progenitors control blood production in normal and regenerative conditions. *Cell Stem Cell*, **17**(1): 35–46.

Rebel VI, Miller CL, Eaves CJ, et al. 1996. The repopulation potential of fetal liver hematopoietic stem cells in mice exceeds that of their liver adult bone marrow counterparts. *Blood*, **87**(8): 3500–3507.

Rodriguez-Fraticelli AE, Weinreb C, Wang SW, et al. 2020. Single-cell lineage tracing unveils a role for TCF15 in haematopoiesis. *Nature*, **583**(7817): 585–589.

Sawai CM, Babovic S, Upadhaya S, et al. 2016. Hematopoietic stem cells are the major source of multilineage hematopoiesis in adult animals. *Immunity*, **45**(3): 597–609.

Stonehouse OJ, Biben C, Weber TS, et al. 2024. Clonal analysis of fetal hematopoietic stem/progenitor cells reveals how post-transplantation capabilities are distributed. *Stem Cell Reports*, **19**(8): 1189–1204.

Street K, Risso D, Fletcher RB, et al. 2018. Slingshot: cell lineage and pseudotime inference for single-cell transcriptomics. *BMC Genomics*, **19**(1): 477.

Weinreb C, Rodriguez-Fraticelli A, Camargo FD, et al. 2020. Lineage tracing on transcriptional landscapes links state to fate during differentiation. *Science*, **367**(6479): eaaw3381.

Wilson A, Laurenti E, Oser G, et al. 2008. Hematopoietic stem cells reversibly switch from dormancy to self-renewal during homeostasis and repair. *Cell*, **135**(6): 1118–1129.

Wilson NK, Kent DG, Buettner F, et al. 2015. Combined single-cell functional and gene expression analysis resolves heterogeneity within stem cell populations. *Cell Stem Cell*, **16**(6): 712–724.

Ye H, Wang XB, Li ZC, et al. 2017. Clonal analysis reveals remarkable functional heterogeneity during hematopoietic stem cell emergence. *Cell Research*, **27**(8): 1065–1068.

Yi SQ, Zhang HF, Sheng Y. 2026. Functions of mitochondrial metabolism in hematopoiesis and hematopoietic malignancies. *Blood Science*, **8**(1): e00271.

Zhang M, Liu D, Lan Y, et al. 2024. Hematopoietic stem cell heterogeneity in non-human primates revealed by five-lineage output bias analysis. *Blood Science*, **6**(1): e00176.